Electronic Supplementary Material (ESI) for Journal of Materials Chemistry C.

Highly flexible dual-mode anti-counterfeiting design based on tunable multi-band emissions and afterglow from chromium doped aluminates

Huanxin Yang,[a] Weiren Zhao,*[,a] Enhai Song,[b] Rui Yun,[c] Hao Huang,[a] Jingzhou Song,[a] Jiyou Zhong,[a] Hui Zhang,[a] Zhaogang Nie,[a] and Yang Li[a]

(Supporting Information)

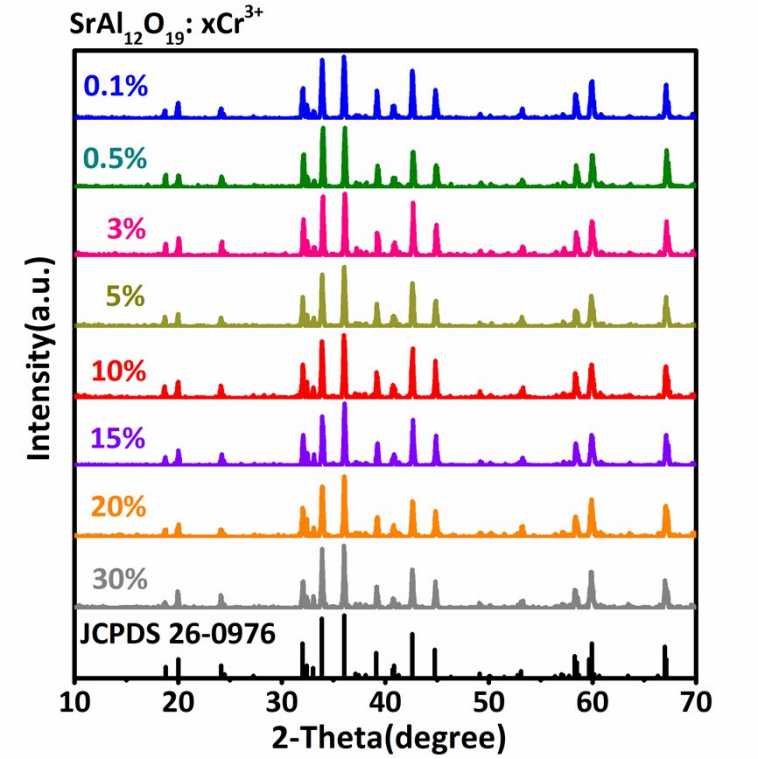

Fig. S1. XRD patterns for $SrAl_{12}O_{19}$: xCr^{3+} (x = 0.1%, 0.5%, 3%, 5%, 10%, 15%, 20%, 30%) phosphors range from 10 to 70 degrees and standard PDF card for the matrix $SrAl_{12}O_{19}$.

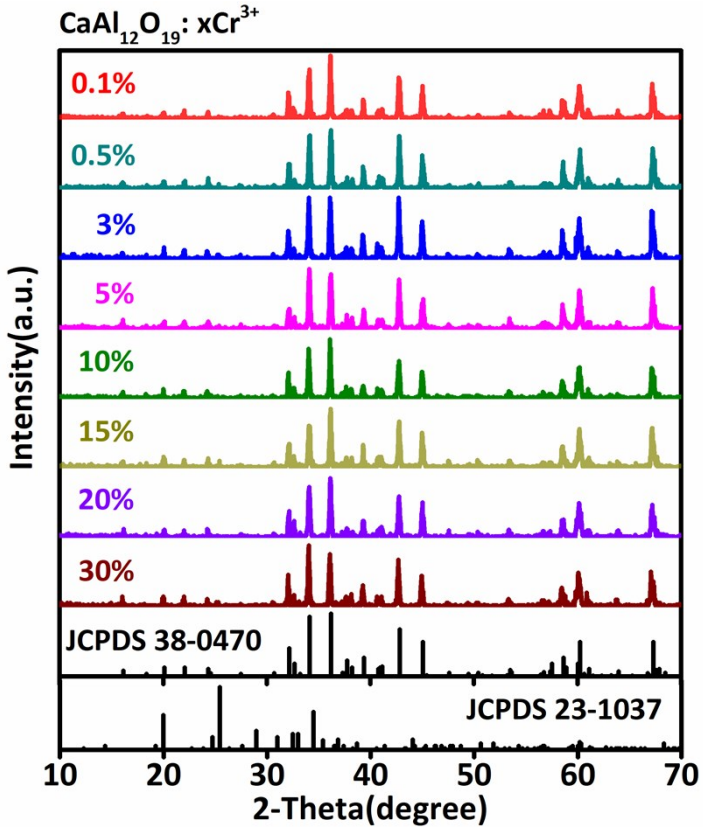

Fig. S2. XRD patterns for $CaAl_{12}O_{19}$: xCr^{3+} (x = 0.1%, 0.5%, 3%, 5%, 10%, 15%, 20%, 30%) phosphors and standard PDF card for the matrix $CaAl_{12}O_{19}$.

The preferred orientation of the crystalline particles shows a little different between phosphors, which may be caused by the Cr^{3+} dopant, or the tiny difference of specific synthesized high temperature. Besides, the weak peak at around 25.427° may be caused by a slight product of $CaAl_4O_7$. But from the subsequent PL spectra and afterglow decay curves, it does not impact the regularity of phosphors.

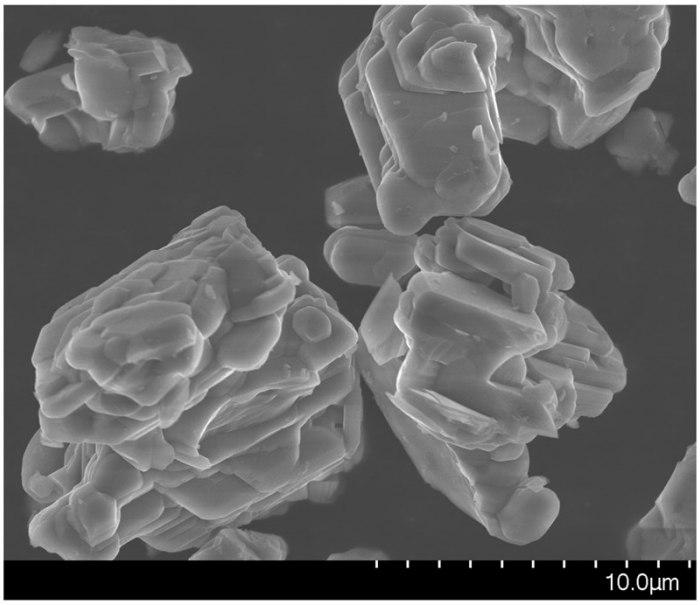

Fig. S3. SEM image of $CaAl_{12}O_{19}$: 0.5%Cr^{3+} microparticles at high magnification.

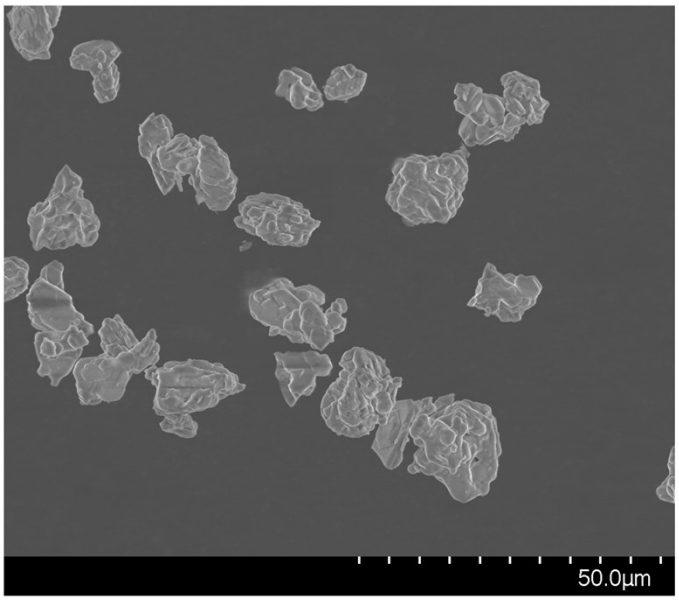

Fig. S4. SEM image of $CaAl_{12}O_{19}$: 0.5%Cr^{3+} microparticles. (at low magnification)

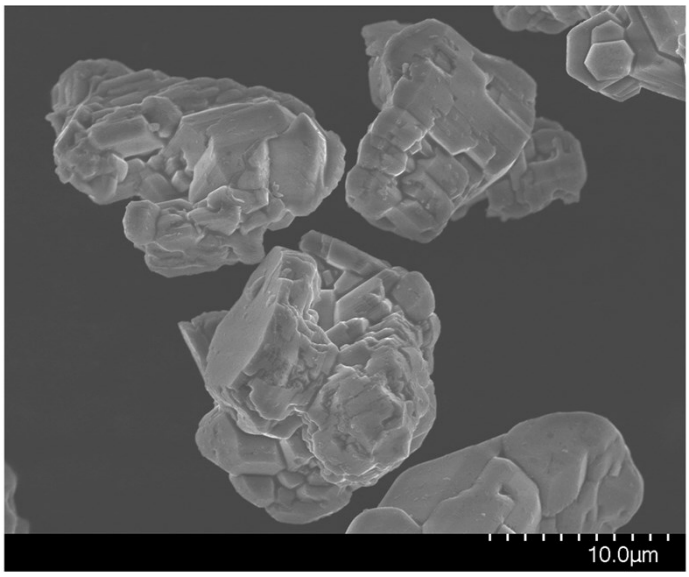

Fig. S5. SEM image of $SrAl_{12}O_{19}$: 0.5%Cr^{3+} microparticles. (at high magnification)

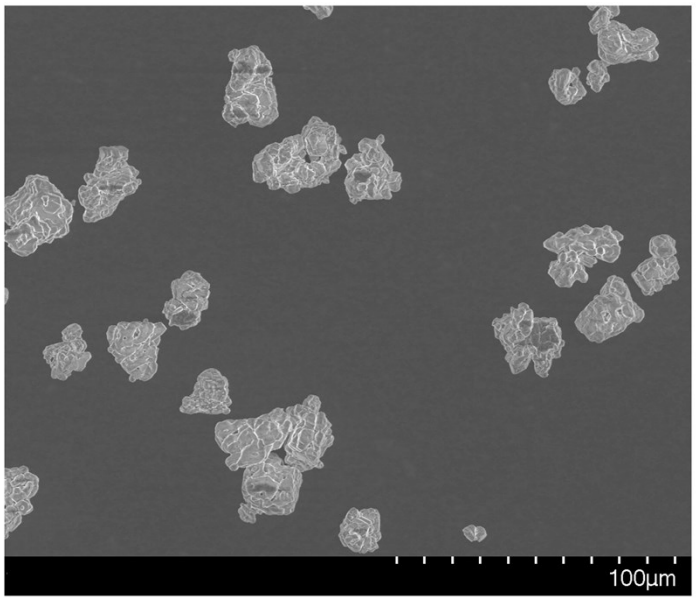

Fig. S6. SEM image of $SrAl_{12}O_{19}$: 0.5%Cr^{3+} microparticles. (at low magnification)

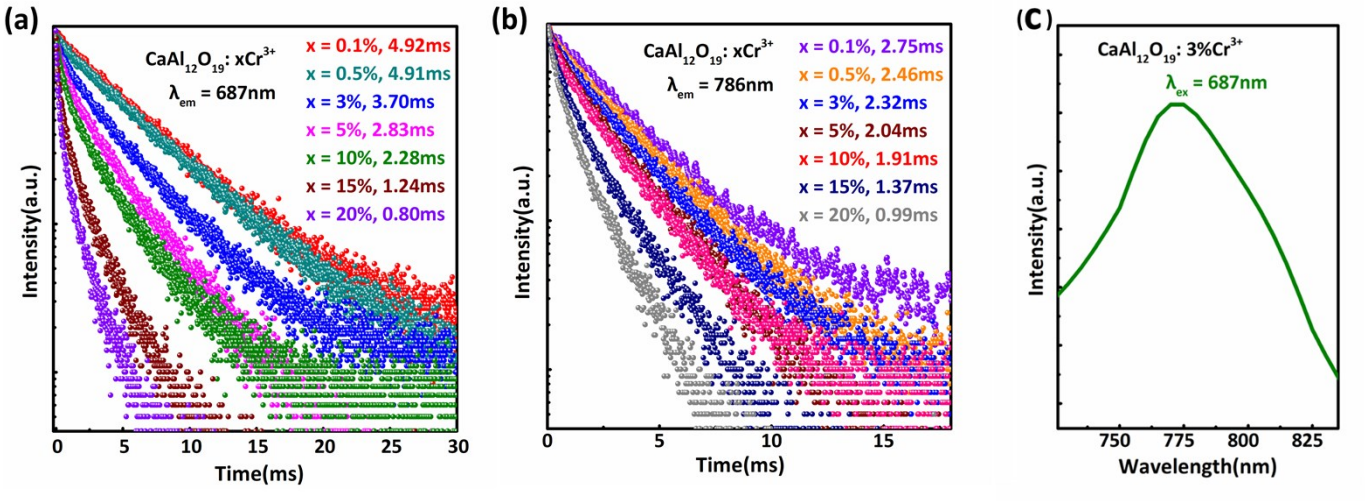

Fig. S7. Fluorescent decay curves of $CaAl_{12}O_{19}$: xCr^{3+} (x = 0.1%-30%) monitoring at (a) 687 and (b) 786 nm; (c) Photoluminescence emission spectrum of $CaAl_{12}O_{19}$: 3%Cr^{3+} excited at 687 nm.

We have also measured the emission spectrum excited at 687 nm, shown as Figure S7c. Obviously, the broad emission band can be excited by the 687 nm deep red light ($^4A_2 \rightarrow {}^2E$ absorption of Cr^{3+} ions). Therefore, it is reasonable to consider that the lifetime may be affected by the energy transfer or reabsorption between two types of Cr^{3+} ions. (Refs. 14, 15 and 31) So, the emission peaks show double exponential decay behavior at the heavy concentration of Cr^{3+} (3%-20%). At the low concentration (0.1% and 0.5%), the intensity of broad emission is too weak to cause obvious energy transfer. Therefore, the only single exponential fitting is used.

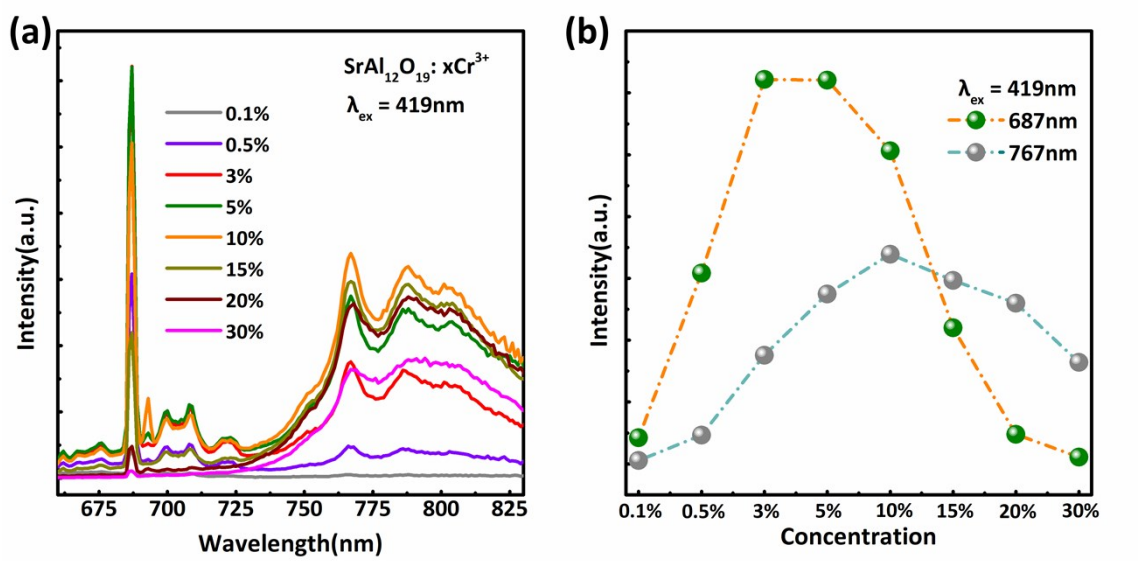

Fig. S8. (a) PL spectra of $SrAl_{12}O_{19}$: xCr^{3+} (x = 0.1%-20%) phosphors range from 650 to 830 nm under the excitation at 419 nm; (b) Variation of the emission intensity of 687 (green balls) and 767 nm (gray balls) with the concentration of Cr^{3+} dopant in $SrAl_{12}O_{19}$ matrix.

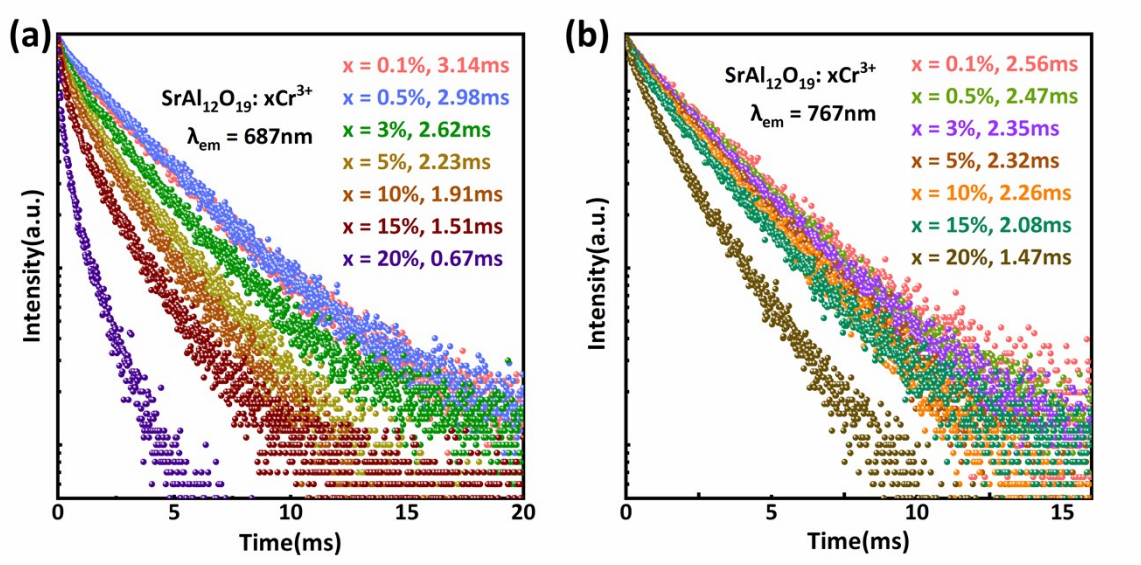

Fig. S9. Fluorescent decay curves of $SrAl_{12}O_{19}$: xCr^{3+} (x = 0.1%-20%) monitoring at (a) 687 and (b) 767 nm.

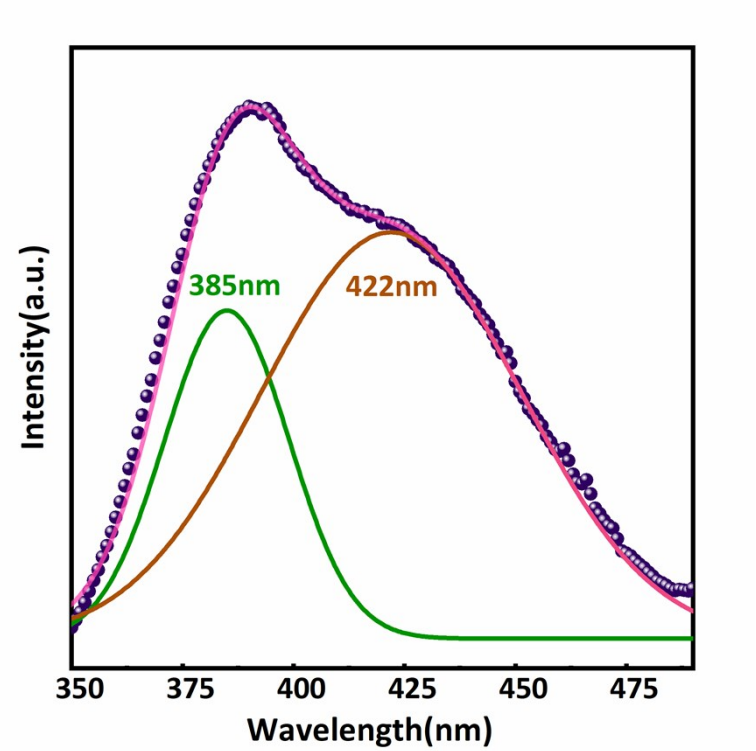

Fig. S10. PLE spectrum (350-490 nm) of $CaAl_{12}O_{19}$: 0.5%Cr^{3+} phosphor by monitoring 786 nm emission and its Gaussian fitting curves.

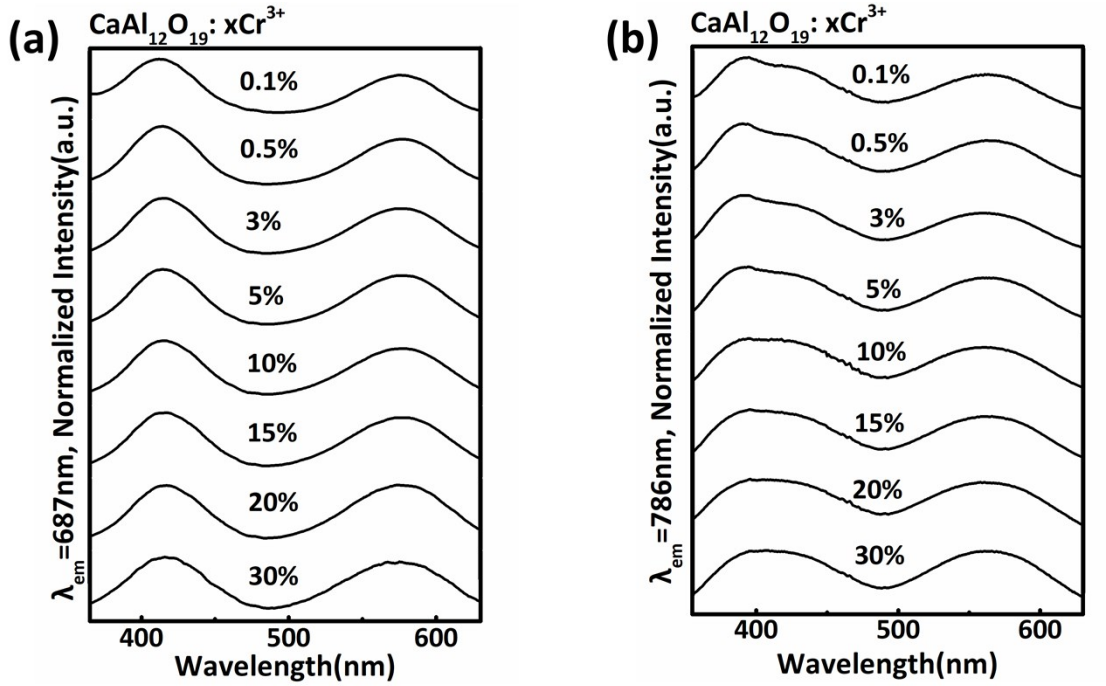

Fig. S11. Normalized PLE spectra of $CaAl_{12}O_{19}$: xCr^{3+} (x = 0.1%, 0.5%, 3%, 5%, 10%, 15%, 20%, 30%) by monitoring (a) 687 and (b) 786 nm emissions.

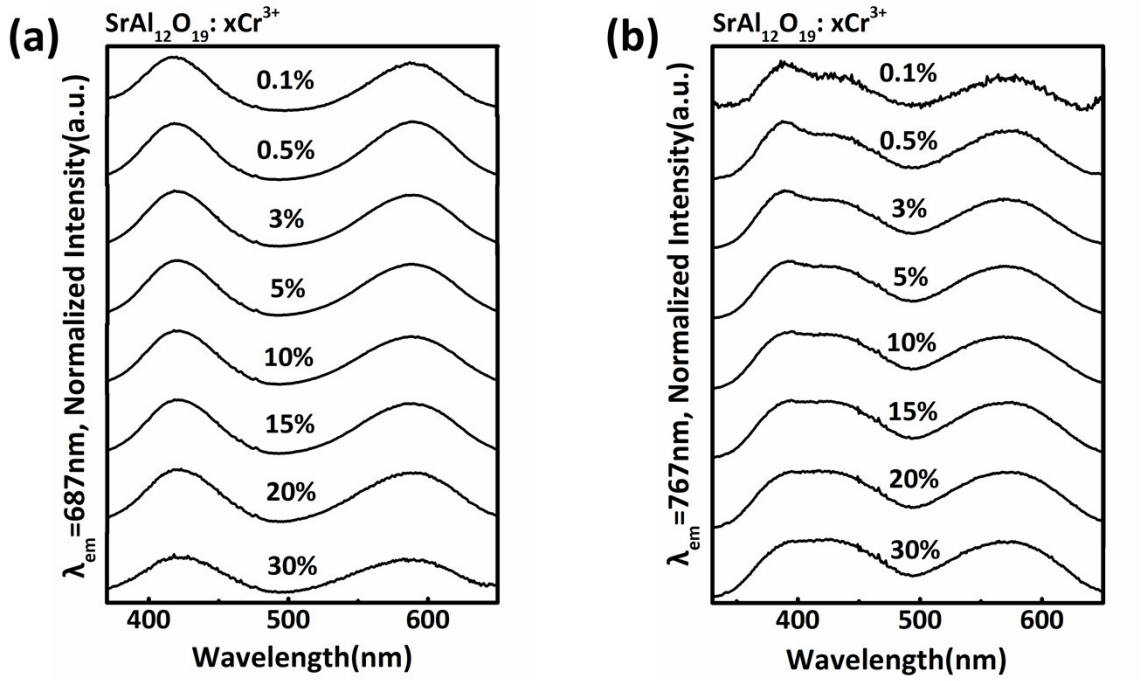

Fig. S12. Normalized PLE spectra of $SrAl_{12}O_{19}$: xCr^{3+} (x = 0.1%, 0.5%, 3%, 5%, 10%, 15%, 20%, 30%) by monitoring (a) 687 and (b) 767 nm emissions.

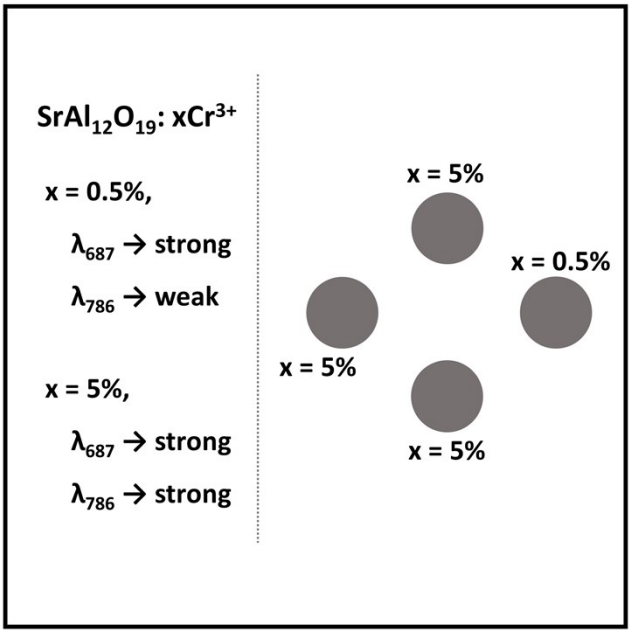

Fig. S13. Fluorescent mode anti-counterfeiting information design schematic by using $SrAl_{12}O_{19}$: 0.5%Cr^{3+} and 5%Cr^{3+} phosphors.

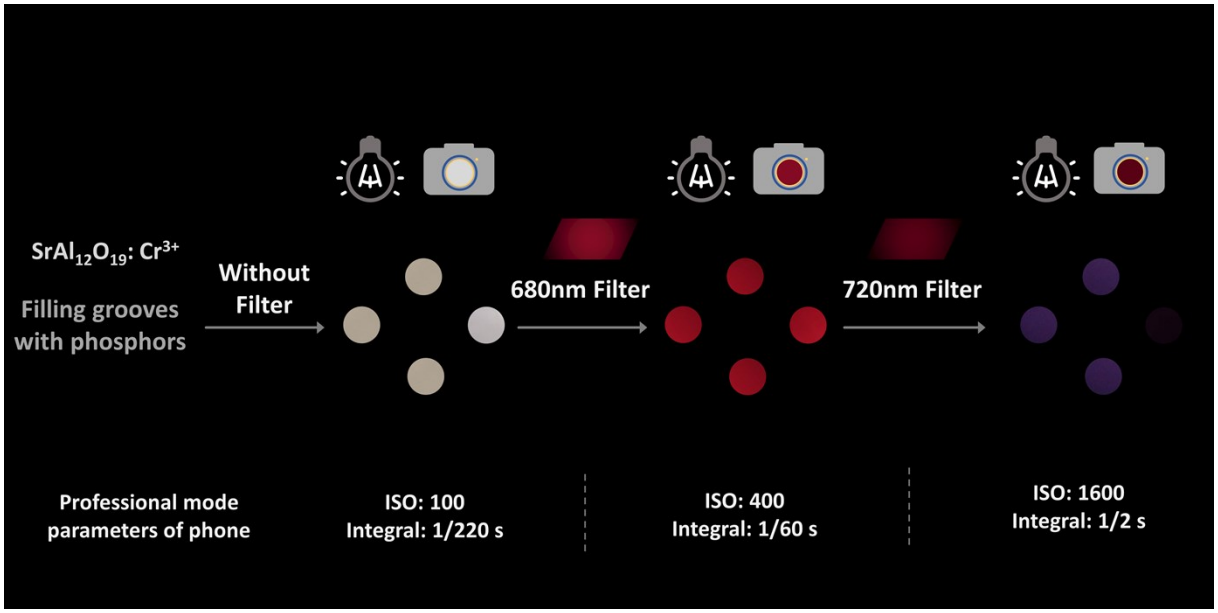

Fig. S14. Actual anti-counterfeiting effect of $SrAl_{12}O_{19}$: 0.5% Cr^{3+} and 5%Cr^{3+} realized through matrix circles and reading process by using corresponding filters.

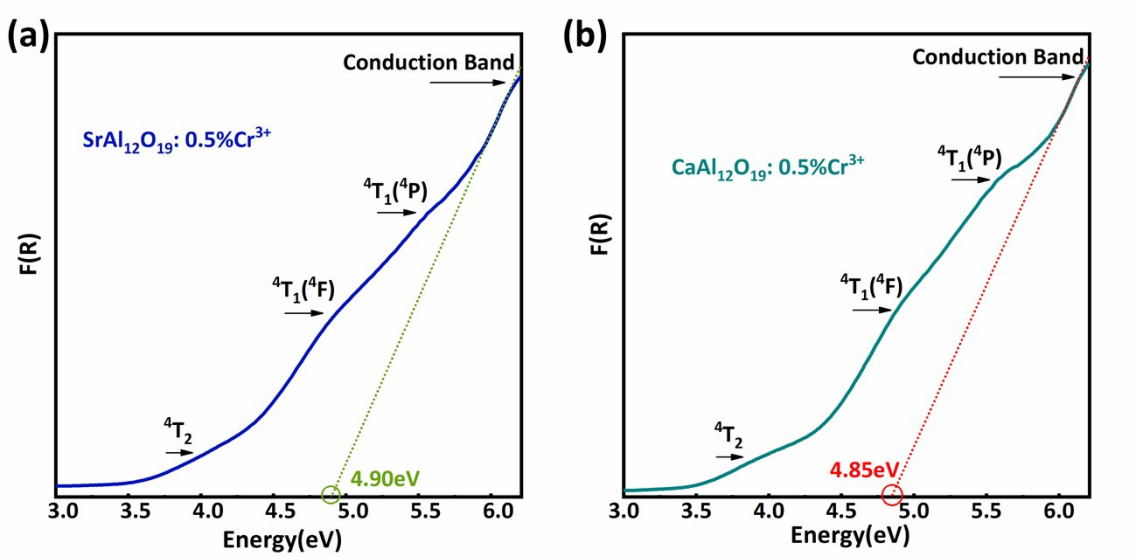

Fig. S15. Converted absorption spectra of (a) $SrAl_{12}O_{19}$: 0.5%Cr^{3+} and (b) $CaAl_{12}O_{19}$: 0.5%Cr^{3+} phosphors via Kubelka-Munk function F(R). The corresponding bandgap energy for the phosphors is estimated from the intercept of fitted straight line (green dots for $SrAl_{12}O_{19}$: 0.5%Cr^{3+}, and red dots for $CaAl_{12}O_{19}$: 0.5%Cr^{3+}).

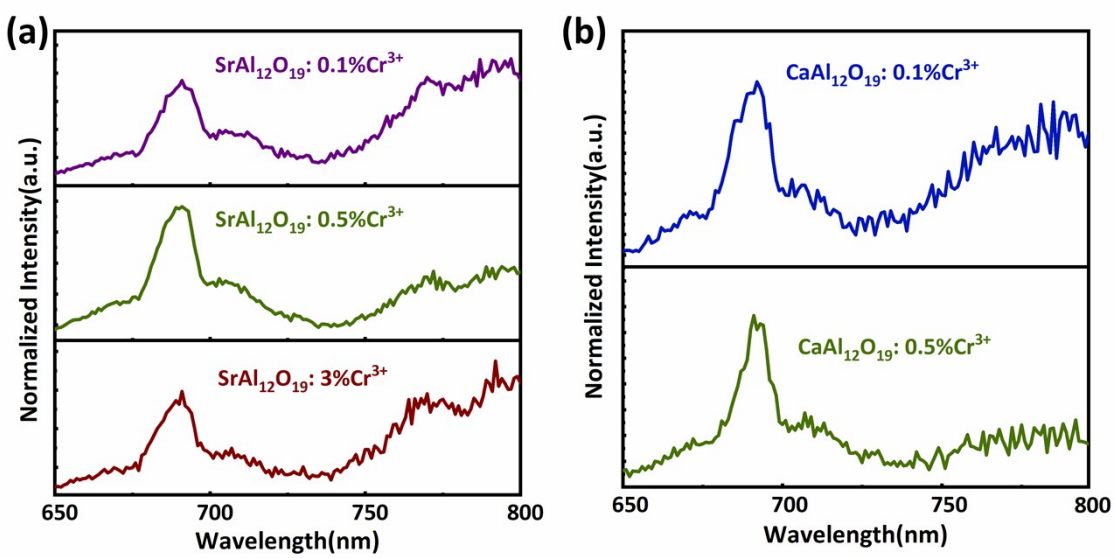

Fig. S16. (a) Afterglow emission spectra range from 650 to 800 nm of $SrAl_{12}O_{19}$: 0.1%, 0.5% and 3% Cr^{3+} phosphors; (b) Afterglow emission spectra range from 650 to 800 nm of $CaAl_{12}O_{19}$: 0.1% and 0.5% Cr^{3+} phosphors.

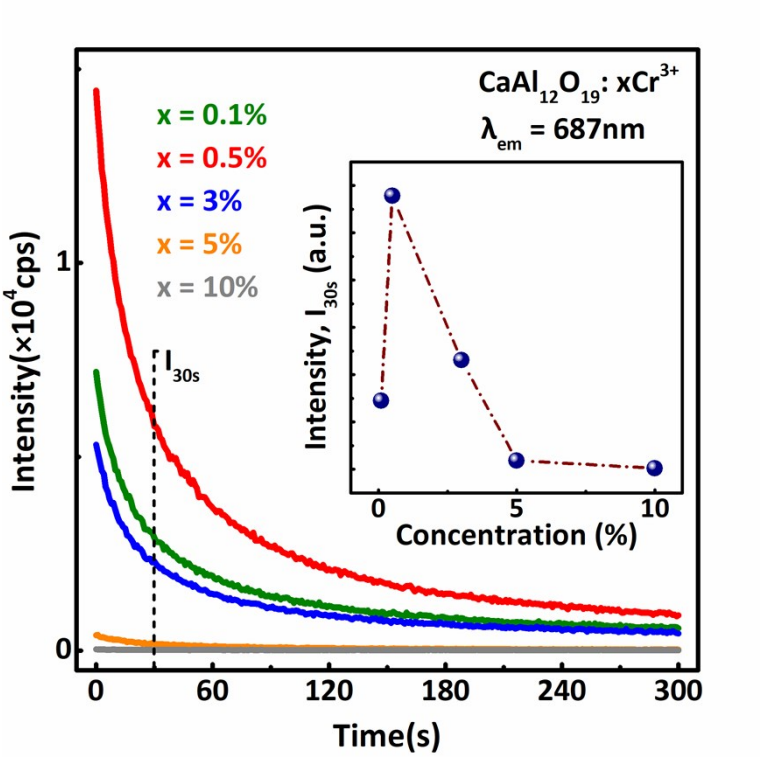

Fig. S17. Afterglow decay curves of $CaAl_{12}O_{19}$: xCr^{3+} (x = 0.1%-10%) phosphors monitoring at 687 nm. (All phosphors are pre-charging by 15 W, 254 nm UV lamp for 5 min)

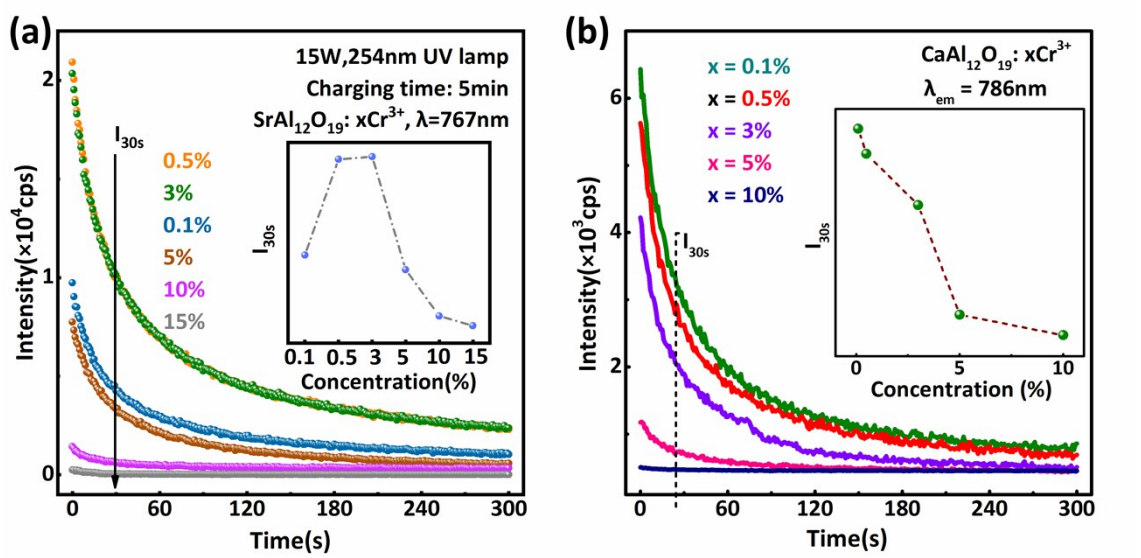

Fig. S18. (a) Afterglow decay curves of $SrAl_{12}O_{19}$: xCr^{3+} (x = 0.1%-15%) phosphors monitoring at 767 nm; (b) Afterglow decay curves of $CaAl_{12}O_{19}$: xCr^{3+} (x = 0.1%-10%) phosphors monitoring at 786 nm. (All phosphors are pre-charging by 15 W, 254 nm UV lamp for 5 min) All illustrations are concentration dependent afterglow intensity at 30 s.

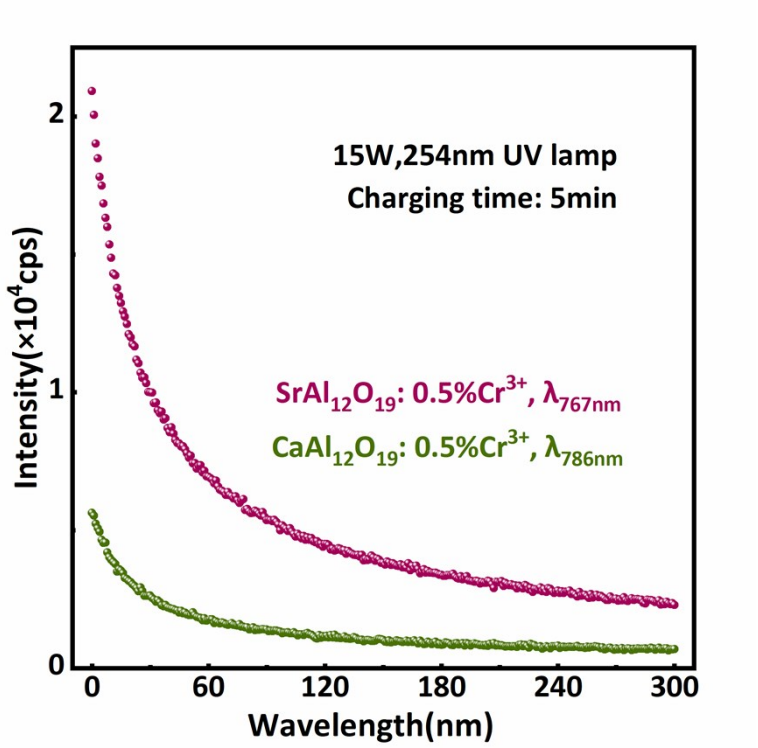

Fig. S19. Afterglow decay curves comparation between $CaAl_{12}O_{19}$: 0.5%Cr^{3+} and $SrAl_{12}O_{19}$: 0.5%Cr^{3+} phosphors monitoring at respective broad band. (767 nm for $SrAl_{12}O_{19}$: 0.5%Cr^{3+} and 786 nm for $CaAl_{12}O_{19}$: 0.5%Cr^{3+})

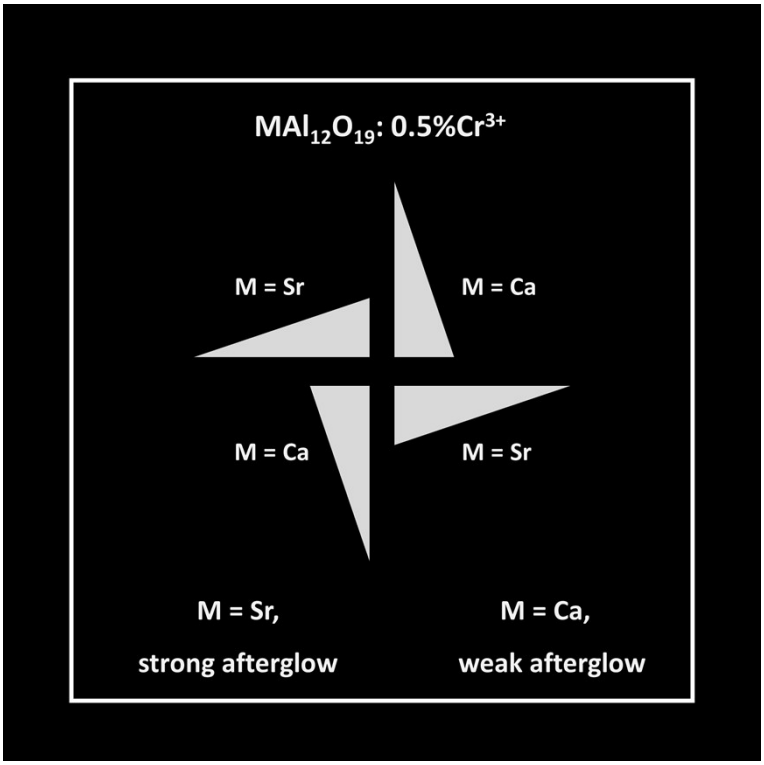

Fig. S20. Mechanism diagram of afterglow anti-counterfeiting by using windmill pattern designment.

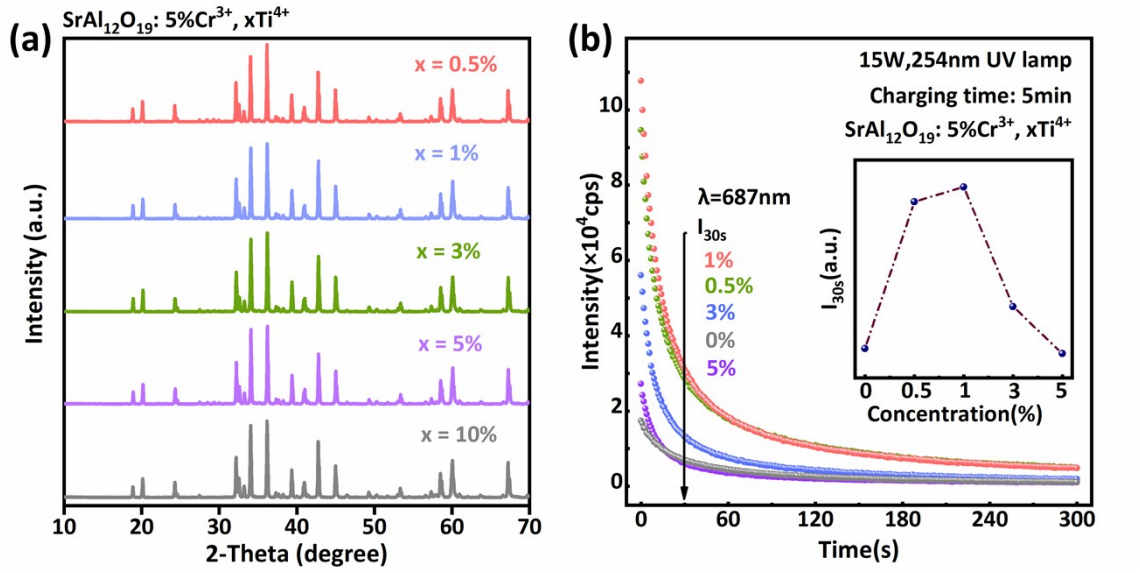

Fig. S21. (a) XRD patterns for $SrAl_{12}O_{19}$: 5%Cr^{3+}, xTi^{4+} (x = 0.5%, 1%, 3%, 5%, 10%) phosphors range from 10 to 70 degrees; (b) Afterglow decay curves of $SrAl_{12}O_{19}$: 5%Cr^{3+}, xTi^{4+} (x = 0, 0.5%, 1%, 3% and 5%) phosphors monitoring at 687 nm. (All phosphors are pre-charging by 15 W, 254 nm UV lamp for 5 min). The illustration shows concentration dependent afterglow intensity at 30 s.

The XRD patterns for $SrAl_{12}O_{19}$: 5%Cr^{3+}, xTi^{4+} (x = 0.5%, 1%, 3%, 5%, 10%) phosphors show that the co-dopant Ti^{4+} dose not obviously affect the lattice of matrix.

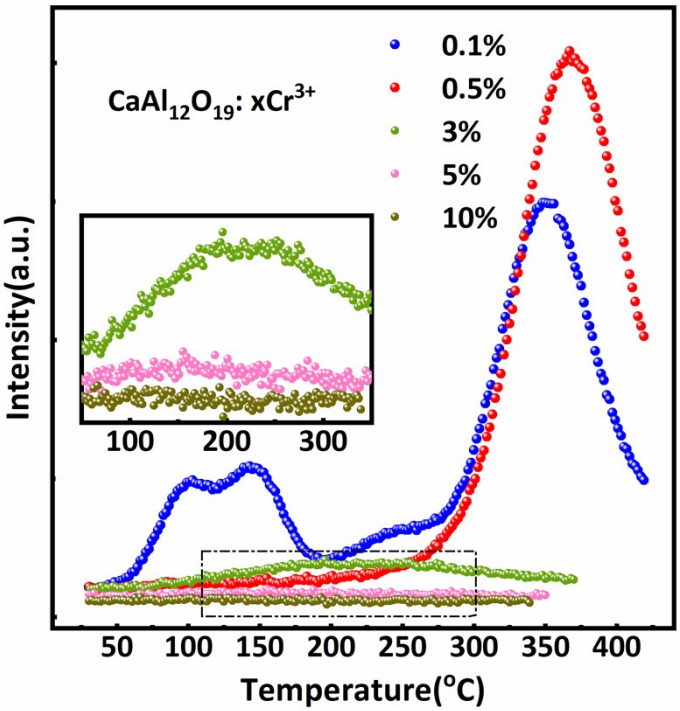

Fig. S22. Thermal-Luminescence (TL) curves of $CaAl_{12}O_{19}$: xCr^{3+} (x = 0.1%-10%) phosphors. The illustration is a close-up of the 50–350 °C image in the original picture. Before each measurement, the phosphor has been pre-irradiated by UV lamp for 5 min.

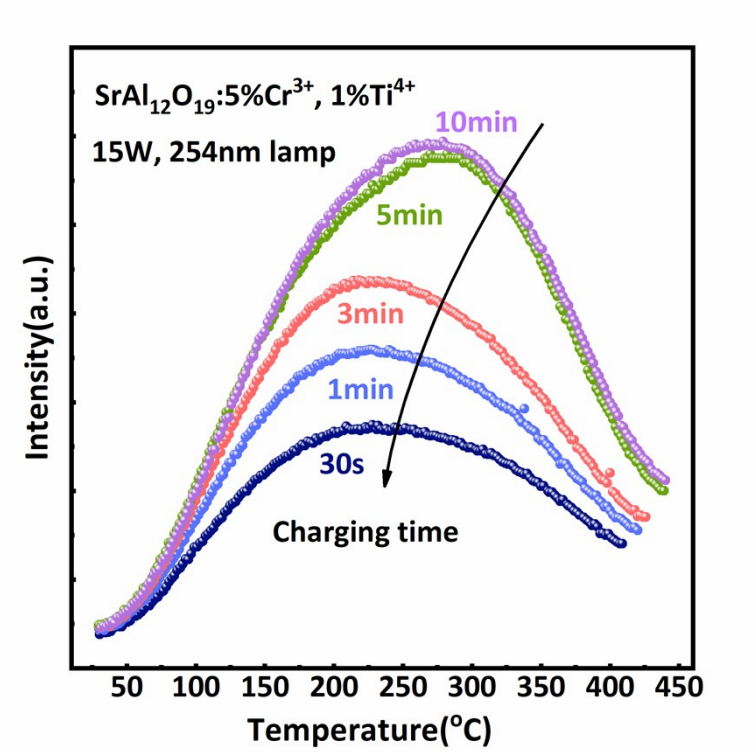

Fig. S23. TL curves of $SrAl_{12}O_{19}$: 5%Cr^{3+}, 1%Ti^{4+} phosphor charging by 15 W, 254 nm for different time (30 s, 1, 3, 5, 10 min), and waiting time is 1 min after ceasing UV lamp in each measurement.

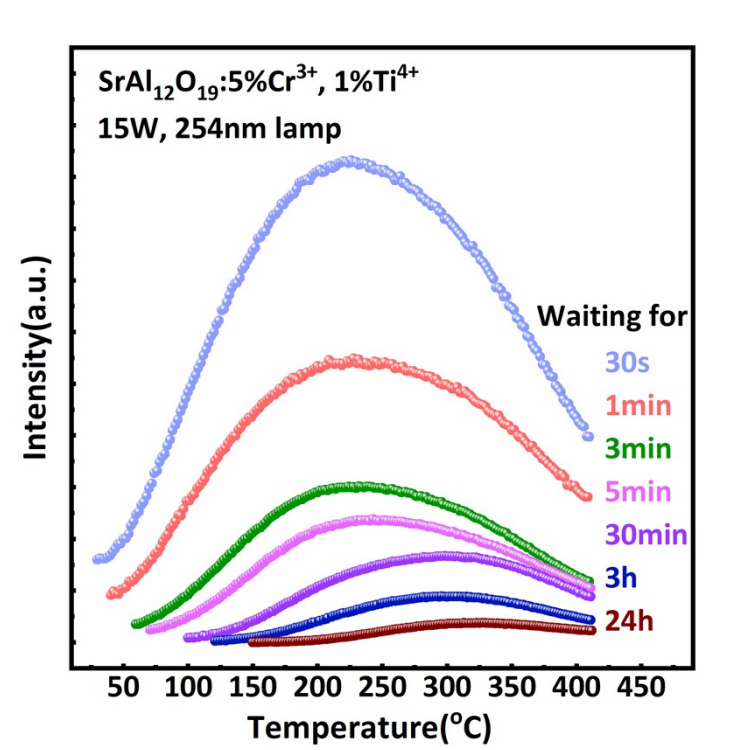

Fig. S24. TL curves of $SrAl_{12}O_{19}$: 5%Cr^{3+}, 1%Ti^{4+} phosphor after ceasing UV lamp for different time (30 s, 1, 3, 5, 30 min, 3 h, 24 h). The UV charging time of all measurements is 5 min.

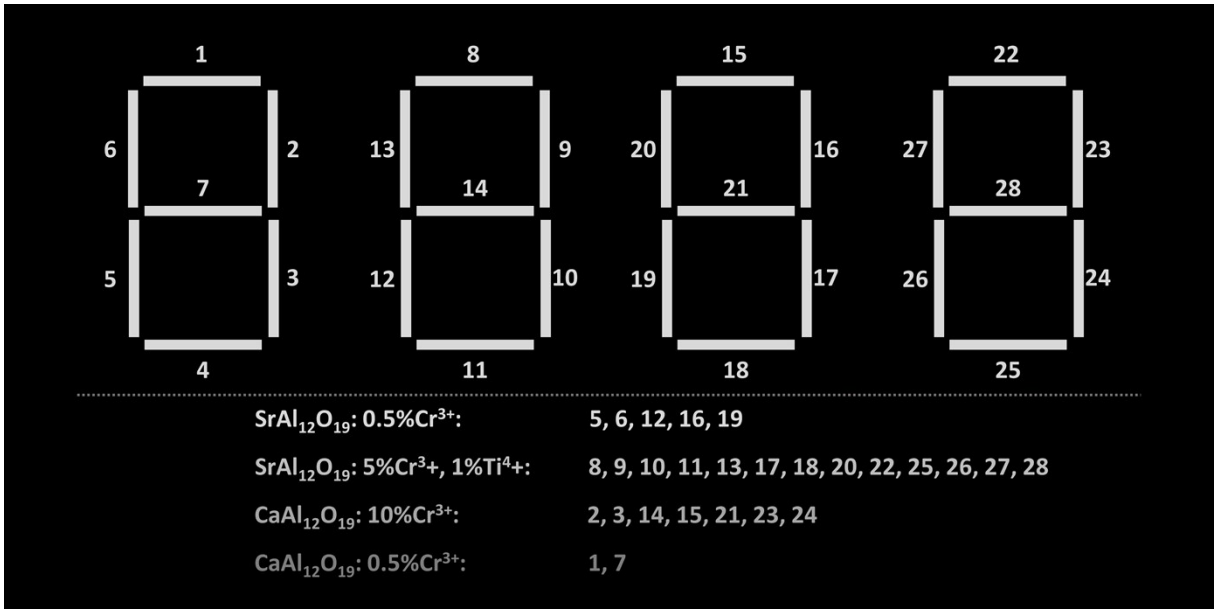

Fig. S25. Dual-mode anti-counterfeiting information design and encryption realized by using four digital tubes shape.

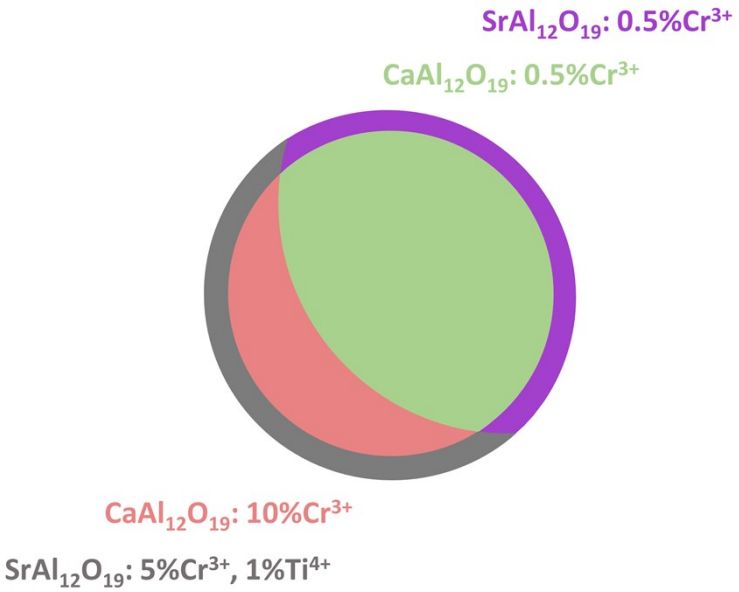

Fig. S26. Design of dual-mode anti-counterfeiting sun, solar eclipse, annular solar eclipse patterns.

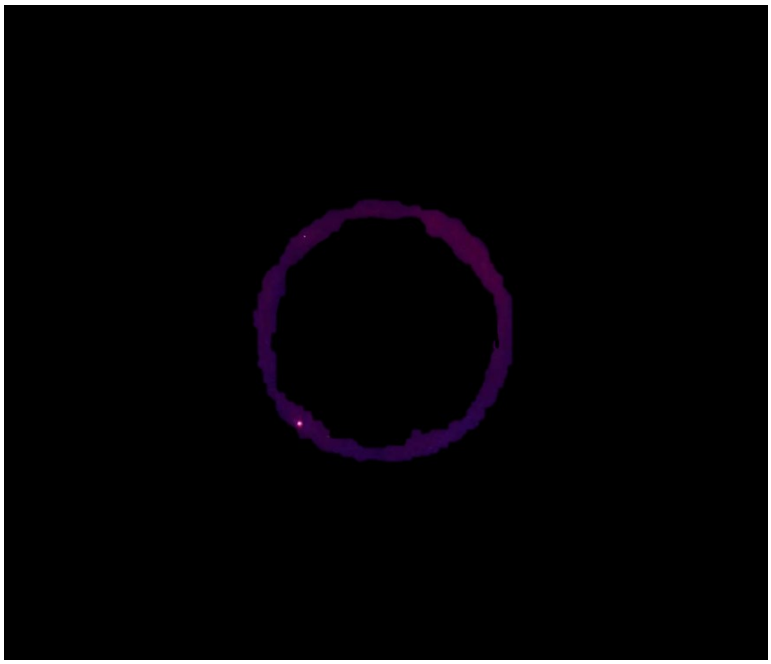

Fig. S27. Afterglow captured after a 4 W, 254 nm lamp excitation for 5 min.

Obviously, although excited by a 4 W UVC lamp, the afterglow still can be captured by our daily used smartphones. Thus, the afterglow mode still can be used even with low power UVC LED chip, which further explain its utility.

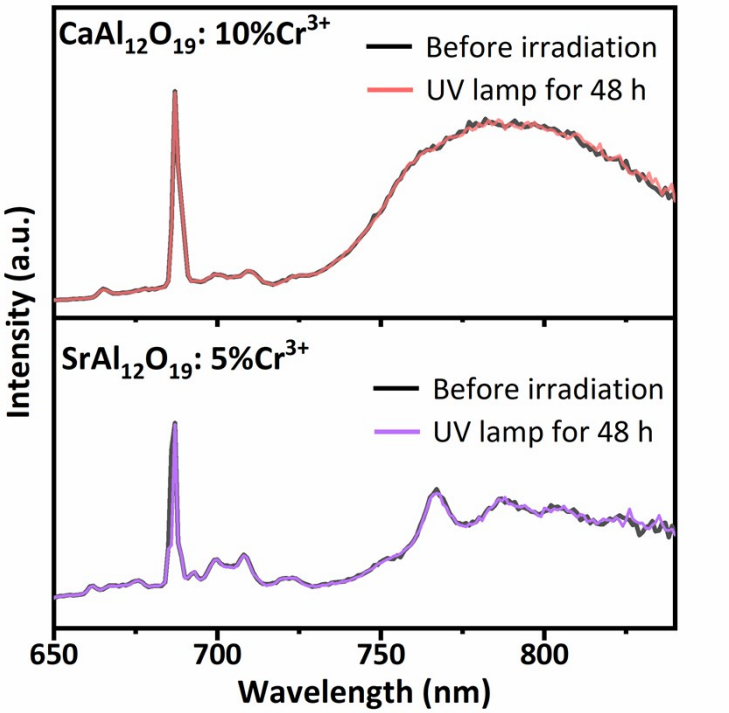

Fig. S28. Photostability of $CaAl_{12}O_{19}$: 10%Cr^{3+} and $SrAl_{12}O_{19}$: 5%Cr^{3+} phosphors under 15 W, 254 nm UV lamp for 48 h.

Take the $CaAl_{12}O_{19}$: 10%Cr^{3+} and $SrAl_{12}O_{19}$: 5%Cr^{3+} phosphors as examples. The spectra before and after UV lamp irradiation are almost identical, suggesting that the phosphors have excellent photostability.

Fig. S29. Dual-mode anti-counterfeiting information captured at 50 ^{o}C.

The fluorescent and afterglow information captured at high temperature further explains its valuable application. Remarkably, the afterglow information at high temperature is much clearer than that at room temperature. Because the electrons are easier to be released from the deep traps at higher temperature.